Chiral zero energy modes in two-dimensional disordered Dirac semimetals

Lei Liu,[1,2] Yan Yu,[1,3,4] Hai-Bin Wu,[6] Yan-Yang Zhang,[1,4,5,*] Jian-Jun Liu,[6] and Shu-Shen Li[1,4,7]

[1]*SKLSM, Institute of Semiconductors, Chinese Academy of Sciences, P.O. Box 912, Beijing 100083, China*

[2]*Department of Medical Physics, School of Medical Imaging, Hebei Medical University, Shijiazhuang, Hebei 050017, China*

[3]*School of Physical Sciences, University of Chinese Academy of Sciences, Beijing 101408, China*

[4]*Synergetic Innovation Center of Quantum Information and Quantum Physics, University of Science and Technology of China, Hefei, Anhui 230026, China*

[5]*School of Microelectronics, University of Chinese Academy of Sciences, Beijing 101408, China*

[6]*Physics Department, Shijiazhuang University, Shijiazhuang, Hebei 050035, China*

[7]*College of Materials Science and Opto-Electronic Technology, University of Chinese Academy of Sciences, Beijing 101408, China*

(Received 16 November 2017; published 10 April 2018)

The vacancy-induced chiral zero energy modes (CZEMs) of chiral-unitary-class (AIII) and chiral-symplectic-class (CII) two-dimensional (2D) disordered Dirac semimetals realized on a square bipartite lattice are investigated numerically by using the Kubo-Greenwood formula with the kernel polynomial method. The results show that, for both systems, the CZEMs exhibit the critical delocalization. The CZEM conductivity remains a robust constant (i.e., $\sigma_{\mathrm{CZEM}} \approx 1.05e^2/h$), which is insensitive to the sample sizes, the vacancy concentrations, and the numbers of moments of Chebyshev polynomials, i.e., the dephasing strength. For both kinds of chiral systems, the CZEM conductivities are almost identical. However, they are not equal to that of graphene (i.e., $4e^2/\pi h$), which belongs to the chiral orthogonal class (BDI) semimetal on a 2D hexagonal bipartite lattice. In addition, for the case that the vacancy concentrations are different in the two sublattices, the CZEM conductivity vanishes, and thus both systems exhibit localization at the Dirac point. Moreover, a band gap and a mobility gap open around zero energy. The widths of the energy gaps and mobility gaps are increasing with larger vacancy concentration difference. The width of the mobility gap is greater than that of the band gap, and a δ-function-like peak of density of states emerges at the Dirac point within the band gap, implying the existence of numerous localized states.

DOI: 10.1103/PhysRevB.97.155302

I. INTRODUCTION

Since Anderson localization phenomenon was revealed in 1958 [1], the effects of disorder on electronic states have been an enduring and important theme, which relates to the fundamental principle and application of quantum mechanics. On the other hand, Dirac and topological matters have recently attracted great attention due to their novel properties. In particular, their electronic states can strongly resist localization in the presence of disorder [2–5].

The disorder-induced Anderson localization transition has several universality classes analogous to the same concept in phase transition theory. Based on the two basic symmetries, i.e., time reversal and spin rotation, the early threefold Wigner-Dyson classification scheme [6,7] includes orthogonal class (with preserved time-reversal symmetry and preserved spin-rotation symmetry), unitary class (with broken time-reversal symmetry), and symplectic class (with preserved time-reversal symmetry and broken spin-rotation symmetry). Further, when one of the additional symmetries, i.e., the chiral or the particle-hole symmetry, is considered, a complete set of universality classes includes, in addition to the three Wigner-Dyson classes, three chiral classes and four Bogoliubov-de Gennes classes. This is known as tenfold Altland-Zirnbauer classification [8–10].

In condensed matter physics, the tight-binding models on a bipartite lattice with nearest-neighbor hoppings (e.g., graphene), even with randomness in these hoppings (e.g., vacancy defects), possess chiral symmetry [6,11,12] because the corresponding Hamiltonian matrices can be written in the form of the block off-diagonal structure,

$$H = \begin{pmatrix} 0 & h \\ h^{\dagger} & 0 \end{pmatrix}, \tag{1}$$

in the sublattice space, i.e., they satisfy the relation

$$\tau^z H \tau^z = -H, \tag{2}$$

where τ^z is the third Pauli matrix in the sublattice space. Graphene with randomly distributed vacancies possesses chiral, time-reversal, and spin-rotation symmetries, and therefore it belongs to the chiral orthogonal class (BDI). As infinitely strong scatterers, vacancies remarkably affect the density of states (DOS) near the Dirac point, leading to the appearance of chiral zero energy modes (CZEMs) [13–19]. CZEMs exhibit critical delocalization, which is related to the universal minimal conductivity of graphene in the clean limit [20–29]. By means of accurate large-scale numerical calculations, Ferreira *et al.* [13] found that the Kubo conductivity of CZEMs induced by vacancies remain the same as the minimal conductivity of graphene. However, as far as we know, few theoretical studies have been carried out for CZEMs of chiral unitary class (AIII) or chiral symplectic class (CII).

*yanyang@semi.ac.cn

After the experimental fabrication of graphene, more two-dimensional (2D) materials have been predicted and discovered [30–34]. Furthermore, quantum simulations with cold atoms in photonic lattices can be implemented on more systems with gauge field and spin-orbit coupling and open up a new way for the realization and the study of 2D systems with various symmetries [35]. These progress pave the way to the realizations of topological semimetals with certain symmetries. The present work concentrates on the vacancy-induced CZEMs of chiral-unitary-class (AIII) and chiral-symplectic-class (CII) 2D disordered Dirac semimetals. We consider a 2D square bipartite lattice as proposed by Hou [36] and Young *et al.* [37], on which tight-binding Hamiltonians of chiral unitary class (AIII) and chiral symplectic class (CII) can be realized. Within the framework of the tight-binding models, the longitudinal conductivity σ_{xx} can be calculated numerically by using the Kubo-Greenwood formula [42–44] in the linear response approximation with the kernel polynomial method (KPM) [38,40,41]. The results show that, qualitatively similar to those of graphene (i.e., chiral orthogonal class), the vacancy-induced CZEMs also emerge in chiral-unitary-class (AIII) and chiral-symplectic-class (CII) Dirac semimetals. The critical delocalization is displayed in CZEMs. At the Dirac point, the longitudinal conductivity σ_{xx} remains a nonzero value, i.e., $\sigma_{\text{CZEM}} \approx 1.05\frac{e^2}{h}$. This value is insensitive to the sample sizes, the vacancy concentrations, and the numbers of moments of Chebyshev polynomials (corresponding to the inelastic broadening parameter). In other words, it is almost a universal constant over a wide range of parameters we consider. It should be noted that, for the classes AIII and CII Dirac semimetals on a 2D square bipartite lattice, the CZEM conductivities are almost equal to each other (i.e., $1.05\frac{e^2}{h}$). However, they are not equal to that of graphene (i.e., $\frac{4e^2}{\pi h}$), which belongs to the class BDI semimetal on a 2D hexagonal bipartite lattice. In addition, when the vacancy concentrations on two sublattices are different, namely, for the vacancy densities of imbalance between A and B sublattices, we find that the CZEM conductivity disappears and the systems exhibit localization at the Dirac point. The band gaps and mobility gaps emerge in the vicinity of the Dirac point. Moreover, there are a large number of localized states at the Dirac point and in the band tails of the valence and conduction bands as well.

This paper is organized as follows. Section II outlines the theoretical framework, Sec. III gives the results and analysis, Sec. IV summarizes the main findings of our work, and finally Appendix gives a brief overview of the KPM method.

II. MODEL AND METHOD

As the simplest models of the classes AIII and CII Dirac semimetals, both systems considered here are all built on the 2D square bipartite lattice [36,37], including A and B sublattices (i.e., containing one atom A and one atom B in each unit cell), as shown in Fig. 1. The model of the class AIII Dirac semimetals for spinless fermions requires a phase factor γ along with the nearest-neighbor hopping for breaking time-reversal symmetry [see the black arrows in Fig. 1(a)]. The 2D tight-binding Hamiltonian in real space [36] can be written

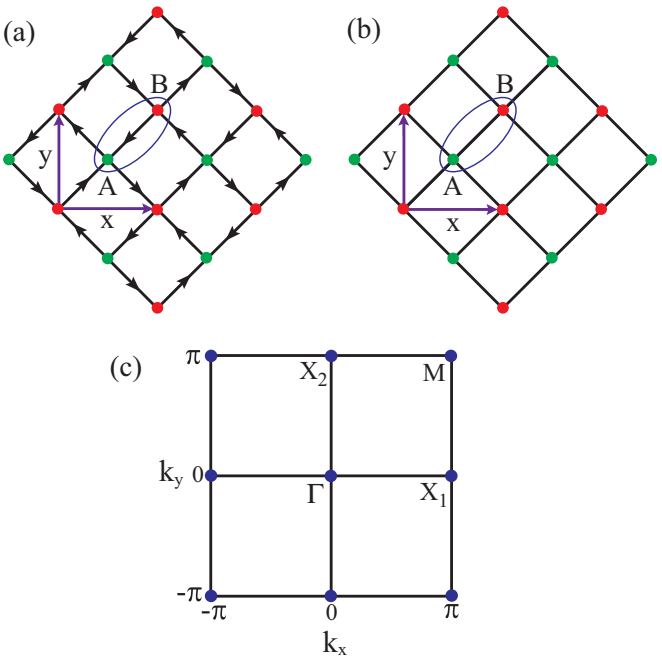

FIG. 1. 2D square bipartite lattice and Brillouin zone. (a) Chiral-unitary-class (AIII) Dirac semimetals. (b) Chiral-symplectic-class (CII) Dirac semimetals. (c) Brillouin zone.

as (setting $\hbar = 1$)

$$H_u = -t\sum_{\boldsymbol{m}\in A} a_{\boldsymbol{m}}^{\dagger}\big[e^{-i\gamma}b_{\boldsymbol{m}+\frac{1}{2}(\hat{\boldsymbol{x}}-\hat{\boldsymbol{y}})} + e^{-i\gamma}b_{\boldsymbol{m}-\frac{1}{2}(\hat{\boldsymbol{x}}-\hat{\boldsymbol{y}})} + e^{i\gamma}b_{\boldsymbol{m}+\frac{1}{2}(\hat{\boldsymbol{x}}+\hat{\boldsymbol{y}})} + e^{i\gamma}b_{\boldsymbol{m}-\frac{1}{2}(\hat{\boldsymbol{x}}+\hat{\boldsymbol{y}})}\big] + \text{H.c.}, \tag{3}$$

where $a_{\boldsymbol{m}}^{\dagger}$ ($b_{\boldsymbol{m}}^{\dagger}$) and $a_{\boldsymbol{m}}$ ($b_{\boldsymbol{m}}$) denote the creation and annihilation operator, respectively, at the lattice site $\boldsymbol{m}$ on sublattice A (B). $\hat{\boldsymbol{x}}$ and $\hat{\boldsymbol{y}}$ indicate the lattice basis vectors of the unit cell shown in Fig. 1(a), t is the hopping energy between the nearest-neighbor sites, and $\gamma = \frac{\pi}{4}$ is the nontrivial hopping phase. Hereafter, we adopt t as the energy unit and the lattice basis vector of the unit cell as the length unit. The band structure of model (3) possesses two inequivalent Dirac points at $X_1 = (\pi,0)$ and $X_2 = (0,\pi)$, respectively, with the same energy, as shown in Fig. 2(a) in momentum space. By performing Fourier transforms $a_{\boldsymbol{k}} = \frac{1}{\sqrt{N}}\sum_{\boldsymbol{m}_a} a_{\boldsymbol{m}_a}e^{-i\boldsymbol{k}\cdot\boldsymbol{m}_a}$, $b_{\boldsymbol{k}} = \frac{1}{\sqrt{N}}\sum_{\boldsymbol{m}_b} b_{\boldsymbol{m}_b}e^{-i\boldsymbol{k}\cdot\boldsymbol{m}_b}$, and by introducing $\Psi_{\boldsymbol{k}} = (a_{\boldsymbol{k}},b_{\boldsymbol{k}})^T$, the Hamiltonian can be written as $H_u = \sum_{\boldsymbol{k}}\Psi_{\boldsymbol{k}}^{\dagger}\mathcal{H}_u(\boldsymbol{k})\Psi_{\boldsymbol{k}}$ with

$$\mathcal{H}_u(\boldsymbol{k}) = \begin{pmatrix} 0 & h(\boldsymbol{k}) \\ h^*(\boldsymbol{k}) & 0 \end{pmatrix}, \tag{4}$$

where

$$h(\boldsymbol{k}) = -e^{i\gamma}[e^{-i(k_x+k_y)} + e^{-i(2\gamma+k_x)} + e^{-i(2\gamma+k_y)} + 1]. \tag{5}$$

The Hamiltonian matrix (4) does not have diagonal terms in the sublattice space, hence the system possesses the chiral symmetry as defined by Eq. (1). However, the time-reversal symmetry is broken, and therefore the system belongs to the symmetry class AIII.

In order to construct the model of the chiral symplectic class CII, we consider a time-reversal-invariant nearest-neighbor

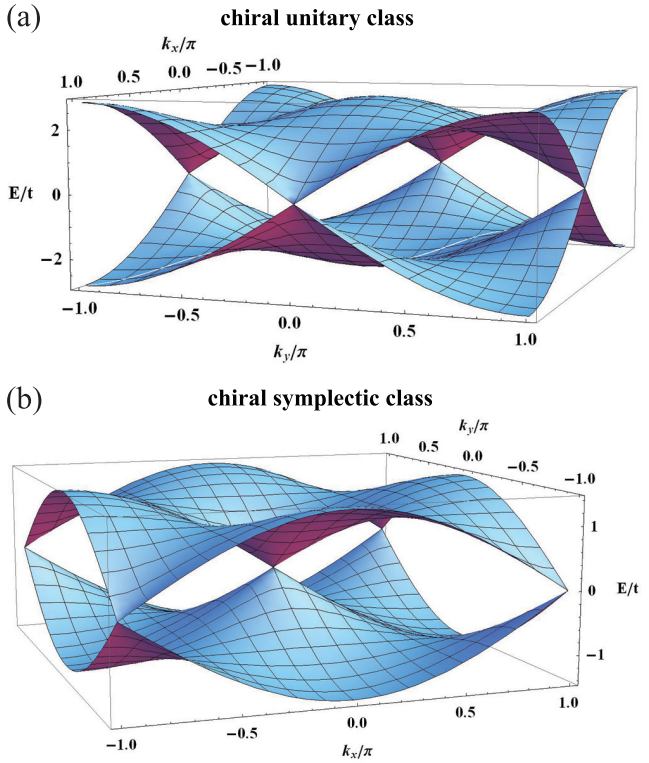

FIG. 2. (a) Dispersion relation of the class AIII Dirac semimetals in the Brillouin zone. (b) Dispersion relation of the class CII Dirac semimetals in the Brillouin zone.

spin-orbit interaction and introduce a Hamiltonian of a 2D Dirac semimetal given by the form in real space:

$$H_s = \frac{t^{\mathrm{SO}}}{2}\Big\{-\sum_{\boldsymbol{m}} a^{\dagger}_{\boldsymbol{m}\downarrow}\big[\big(b_{\boldsymbol{m}+\frac{1}{2}(\hat{\boldsymbol{x}}-\hat{\boldsymbol{y}}),\uparrow} - b_{\boldsymbol{m}-\frac{1}{2}(\hat{\boldsymbol{x}}-\hat{\boldsymbol{y}}),\uparrow}\big) - i\big(b_{\boldsymbol{m}+\frac{1}{2}(\hat{\boldsymbol{x}}+\hat{\boldsymbol{y}}),\uparrow} - b_{\boldsymbol{m}-\frac{1}{2}(\hat{\boldsymbol{x}}+\hat{\boldsymbol{y}}),\uparrow}\big)\big] + \sum_{\boldsymbol{m}} a^{\dagger}_{\boldsymbol{m}\uparrow}\big[\big(b_{\boldsymbol{m}+\frac{1}{2}(\hat{\boldsymbol{x}}-\hat{\boldsymbol{y}}),\downarrow} - b_{\boldsymbol{m}-\frac{1}{2}(\hat{\boldsymbol{x}}-\hat{\boldsymbol{y}}),\downarrow}\big) + i\big(b_{\boldsymbol{m}+\frac{1}{2}(\hat{\boldsymbol{x}}+\hat{\boldsymbol{y}}),\downarrow} - b_{\boldsymbol{m}-\frac{1}{2}(\hat{\boldsymbol{x}}+\hat{\boldsymbol{y}}),\downarrow}\big)\big] + \mathrm{H.c.}\Big\}, \tag{6}$$

where the spin indices $\uparrow$ and $\downarrow$ refer to spin up and spin down, respectively, and t^{SO} denotes the nearest-neighbor hopping parameter with spin flip. We also set $t^{\mathrm{SO}} = 1$ for simplicity. As shown in Fig. 2(b), the dispersion relation of Hamiltonian (6) exhibits two degenerate inequivalent Dirac points at $M = (\pi,\pi)$ and $\Gamma = (0,0)$, respectively. Performing the Fourier transforms $a_{\boldsymbol{k}\uparrow(\downarrow)} = \frac{1}{\sqrt{N}}\sum_{\boldsymbol{m}_a} a_{\boldsymbol{m}_a\uparrow(\downarrow)} e^{-i\boldsymbol{k}\cdot\boldsymbol{m}_a}$, $b_{\boldsymbol{k}\uparrow(\downarrow)} = \frac{1}{\sqrt{N}}\sum_{\boldsymbol{m}_b} b_{\boldsymbol{m}_b\uparrow(\downarrow)} e^{-i\boldsymbol{k}\cdot\boldsymbol{m}_b}$, and introducing $\Psi_{\boldsymbol{k}} = (a_{\boldsymbol{k}\uparrow}, b_{\boldsymbol{k}\uparrow}, a_{\boldsymbol{k}\downarrow}, b_{\boldsymbol{k}\downarrow})^T$, the momentum-space Hamiltonian takes the form $H_s = \sum_{\boldsymbol{k}} \Psi^{\dagger}_{\boldsymbol{k}} \mathcal{H}_s(\boldsymbol{k}) \Psi_{\boldsymbol{k}}$ with

$$\mathcal{H}_s(\boldsymbol{k}) = \tau_x \otimes (\sigma_y \sin k'_x - \sigma_x \sin k'_y) = \begin{pmatrix} 0 & 0 & 0 & K \\ 0 & 0 & K & 0 \\ 0 & K^* & 0 & 0 \\ K^* & 0 & 0 & 0 \end{pmatrix}, \tag{7}$$

where $K = -(i \sin k'_x + \sin k'_y)$, with $k'_x = -(k_x - k_y)/2$ and $k'_y = (k_x + k_y)/2$. $\boldsymbol{\tau} = (\tau_x, \tau_y)$ and $\boldsymbol{\sigma} = (\sigma_x, \sigma_y)$ indicate Pauli matrices describing the sublattice and spin degrees of freedom, respectively. Similarly, in Eq. (7), the Hamiltonian matrix also has a block off-diagonal form as required by Eq. (1), thereby possessing the chiral symmetry. Moreover, the system possesses the time-reversal symmetry, but the spin-orbit interaction breaks the spin-rotation symmetry. Consequently, the system belongs to the symmetry class CII [6,7].

In a tight-binding representation, a vacancy (i.e., a missing atom) can be modeled by cutting off all adjacent bonds to a given atom. Consequently, vacancies do not destroy the chiral symmetry of the original model. On the other hand, a vacancy is equivalent to a locally infinite potential. As a result, vacancies strongly affect DOS near the Dirac point, resulting in the emergence of the CZEMs.

In order to investigate the vacancy-induced CZEMs of the above two systems, we numerically calculate their DOS and longitudinal conductivities σ_{xx} using the Kubo-Greenwood formula [13,44–46], which can be derived from the Kubo formula [42,43] in the zero-temperature limit and written in the form

$$\sigma_{xx}(E_F) = \frac{\hbar e^2}{\pi \Omega} \mathrm{Tr}[\mathrm{Im}G^+(E_F - H) v_x \mathrm{Im}G^+(E_F - H) v_x], \tag{8}$$

where Ω is the size (or area) of the system, $v_x = \frac{1}{i\hbar}[r_x, H]$ denotes the x component of the velocity operator and r_x indicates that of the position operator, $G^+ = \frac{1}{E_F + i\eta - H}$ is the retarded Green's function at the Fermi energy E_F and $\eta \to 0^+$ is the energy (inelastic) broadening parameter that is associated with the dephasing strength [47]. The numerical calculation requires that the broadening parameter η should be larger than the mean level spacing δE, i.e., $\eta \gtrsim \delta E$. In addition, the DOS is given by

$$\rho(\varepsilon) = \frac{1}{D} \mathrm{Tr}[\delta(\varepsilon - H)], \tag{9}$$

where ε is the energy of fermions. For both kinds of disordered chiral systems, periodic boundary conditions are imposed.

The validity of the CZEM conductivity calculated here, as in the case of most of the interesting physical quantities, requires the thermodynamic limit, i.e., $\Omega \to \infty$ and $\eta \to 0$, where Ω denotes the size (or area) of the system and η is the energy (inelastic) broadening parameter. Thus, in order to carry out a reliable quantitative investigation, one should make numerical calculations for the system size as large as possible. Moreover, the disorder averaging should be performed for hundreds of disorder configurations. All of this causes the accurate large-scale numerical calculations to be computationally expensive.

In the present paper, we implement numerical calculations using the progressively arisen KPM method. Different from the Chebyshev-polynomial Green function method used by Ferreira *et al.* [13], the KPM expressions of the conductivity and DOS do not depend explicitly on the broadening parameter η, but depend on the number of moments of Chebyshev polynomials (N), which is associated with η, specifically, $N \propto 1/\eta$ [13,38,39]. A brief overview of the KPM method is given in Appendix.

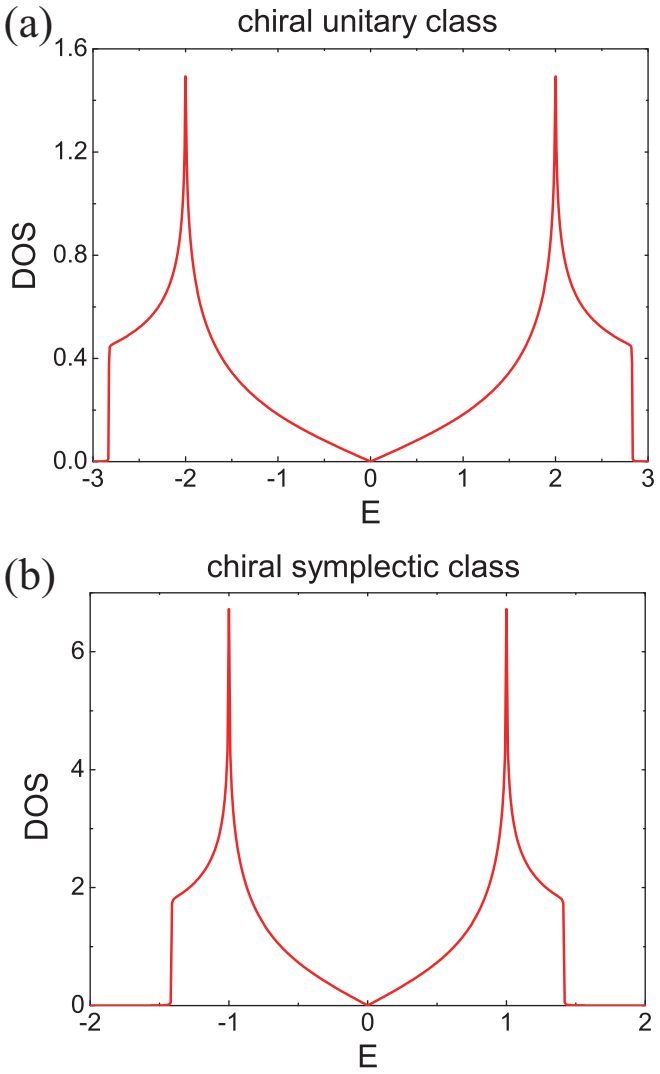

FIG. 3. (a) DOS of pristine class-AIII Dirac semimetals as a function of the energy. (b) DOS of pristine class-CII Dirac semimetals as a function of the energy.

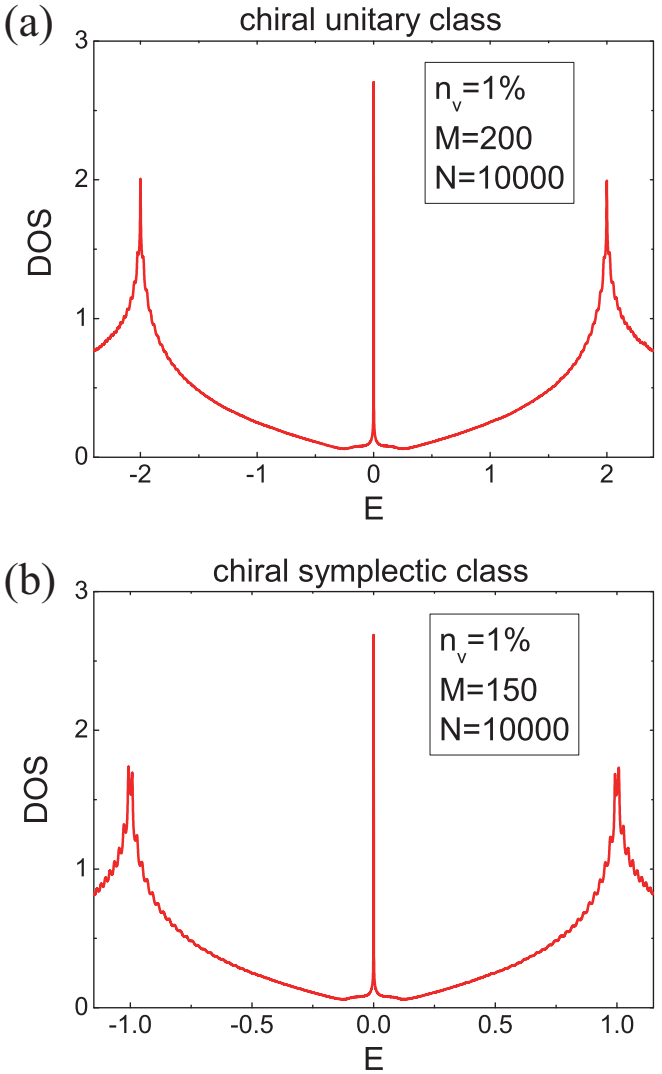

FIG. 4. (a) DOS of disordered class-AIII Dirac semimetals with $2\times200\times200$ sites (i.e., the number of unit cells along x or y direction $M = 200$) as a function of the energy. (b) DOS of disordered class-CII Dirac semimetals with $2\times150\times150$ sites (i.e., the number of unit cells along x or y direction $M = 150$) as a function of the energy. For both systems, the vacancy concentration $n_v = 1\%$, and the number of moments of Chebyshev polynomials $N = 10\,000$.

III. NUMERICAL RESULTS AND DISCUSSIONS

Here we carry out the large-scale numerical calculations for the class AIII and the class CII Dirac semimetals. To ensure a reasonable precision, we employ more than 500 disorder configurations to perform the disorder averaging for each datum computed in this work.

In order to have first impressions for models (3) and (6), we numerically compute the DOS for infinite clean systems in the momentum space using the expression of DOS $\rho(\varepsilon) = -\frac{1}{\pi D}\mathrm{Im}\{\mathrm{Tr}[G^{+}(\varepsilon - H)]\}$. As shown in Fig. 3, for both systems, the DOS is zero at the Dirac point, and the DOS close to the Dirac point depends linearly on the energy, similar to graphene [48].

We next consider the disorder caused by randomly distributed vacancies. In Fig. 4, we show the DOS for disordered systems with the vacancy concentration $n_v = 1\%$. It can be seen that, for both systems, sharp peaks emerge at the Dirac point. This indicates that the randomly distributed vacancies lead to the emergence of numerous quantum states at zero energy in the vicinity of vacancy defects [19], forming the vacancy-induced CZEMs, despite the dilute vacancy concentration $n_v = 1\%$.

In order to investigate the properties of the vacancy-induced CZEMs, we numerically calculate the longitudinal conductivities σ_{xx} using the Kubo-Greenwood formula (8). We find that, as an interesting property of disordered chiral systems, qualitatively similar to those of graphene (i.e., the class BDI) [13], the CZEM conductivities of the classes AIII and CII Dirac semimetals remain a robust constant, which does not vary with the sample sizes, the energy broadening parameter, and even the vacancy concentrations over a wide range of parameters.

In Fig. 5, we first exhibit the longitudinal conductivities of both kinds of disordered chiral systems as functions of the Fermi energy for different numbers of moments of Chebyshev

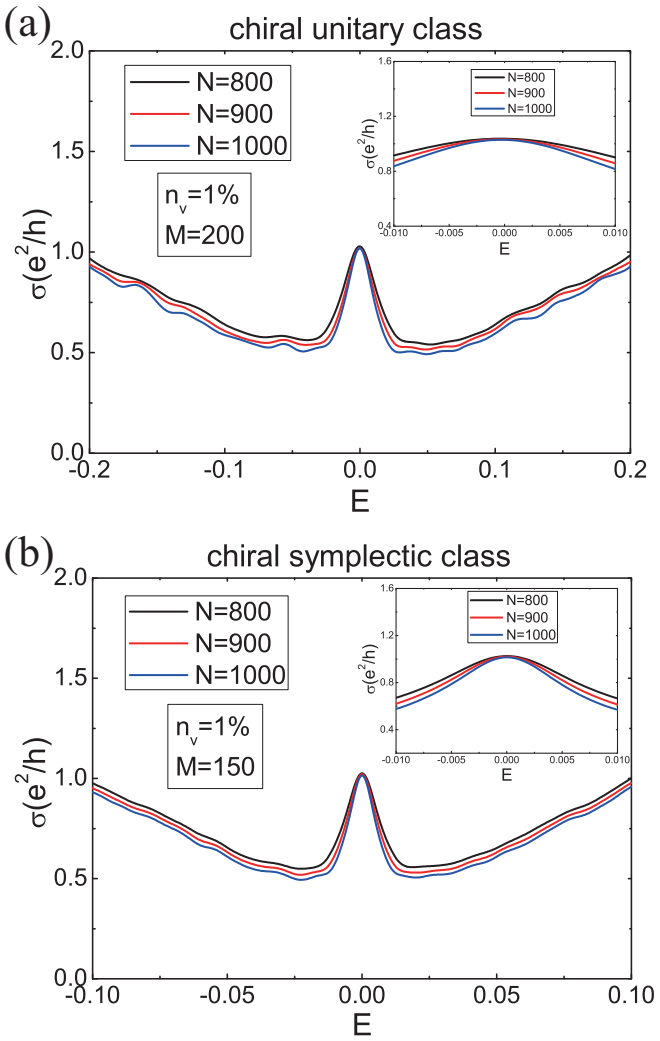

FIG. 5. (a) Longitudinal conductivities of disordered class-AIII Dirac semimetals with $2\times200\times200$ sites as functions of the Fermi energy. (b) Longitudinal conductivities of disordered class-CII Dirac semimetals with $2\times150\times150$ sites as functions of the Fermi energy. For both systems, the black, red, and blue solid curves correspond to the cases of the numbers of moments of Chebyshev polynomials $N = 800$, 900, and 1000, respectively. The vacancy concentration $n_v = 1\%$. The insets show the zooms of peaks at the Dirac points.

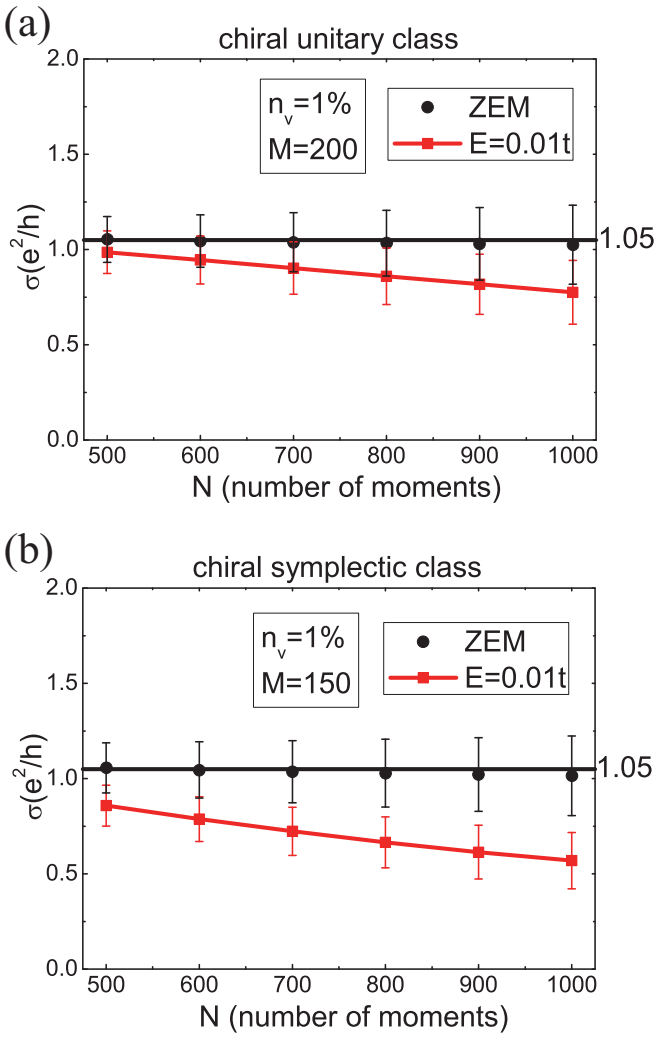

FIG. 6. (a) Longitudinal conductivities of disordered class-AIII Dirac semimetals with $2\times200\times200$ sites as functions of the numbers of moments of Chebyshev polynomials. (b) Longitudinal conductivities of disordered class-CII Dirac semimetals with $2\times150\times150$ sites as functions of the numbers of moments of Chebyshev polynomials. For both systems, the black round dots correspond to the CZEM conductivities at the Dirac points, and the red squares correspond to the case of the Fermi energy $E_F = 0.01t$. The vacancy concentration $n_v = 1\%$. The error bars represent the standard deviation due to disorder average.

polynomials N. Near the Dirac points but except for the Dirac points, the longitudinal conductivities decrease as N increases. This can also be seen clearly in Fig. 6. The longitudinal conductivities at $E_F = 0.01t$ (red squares) indeed decrease with increasing N. This indicates that, during the process of approaching the thermodynamic limit, i.e., $\eta \approx \delta E \to 0$, the localization effects become more and more important.

Most interesting features emerge at the Dirac points associated with the CZEM. In Fig. 6, the conductivity σ_{xx} at $E_F = 0$ (black round dots) almost remains a constant, i.e., $\sigma_{\text{CZEM}} \approx 1.05\frac{e^2}{h}$, for N ranging from 500 to 1000. These results imply the following two facts about the CZEMs. First, for both disordered chiral systems, the conductivities at the Dirac points are insensitive to dephasing [47]. Secondly, the conductivities at the Dirac points approach a fixed value in the thermodynamic and quantum mechanical limits. These results also indicate that, for the Fermi energy $E_F = 0$, the critical delocalization of the CZEMs is protected by the chiral symmetry. This robust conductivity at the Dirac point implies the existence of a quantum critical point [13,49].

Now we concentrate on the fluctuations of conductivities. For example, as shown in Fig. 6, for the CZEM conductivities (black error bars) for the numbers of moments of Chebyshev polynomials $N = 500$, the standard deviations are 0.12038 for the class-AIII Dirac semimetals, and 0.13109 for the class-CII Dirac semimetals, corresponding to 11.4% and 12.4% of the average values, respectively. The error bars increase slowly with increasing N because the matrices $T_n(\tilde{H})$ (shown in

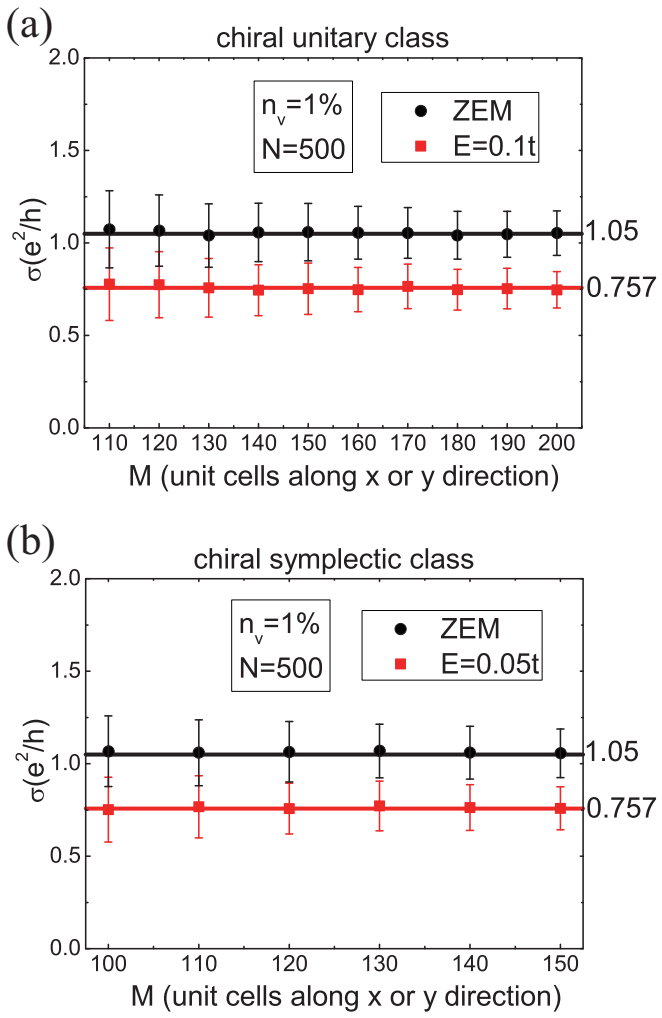

FIG. 7. (a) Longitudinal conductivities of disordered class-AIII Dirac semimetals as functions of the sample sizes. The black round dots correspond to the CZEM conductivities at the Dirac point. The red squares correspond to the case of the Fermi energy $E_F = 0.1t$. (b) Longitudinal conductivities of disordered class-CII Dirac semimetals as functions of the sample sizes. The black round dots correspond to the CZEM conductivities at the Dirac point. The red squares correspond to the case of the Fermi energy $E_F = 0.05t$. For both systems, the vacancy concentration $n_v = 1\%$, and the number of moments of Chebyshev polynomials $N = 500$. The error bars stand for the standard deviation due to disorder average.

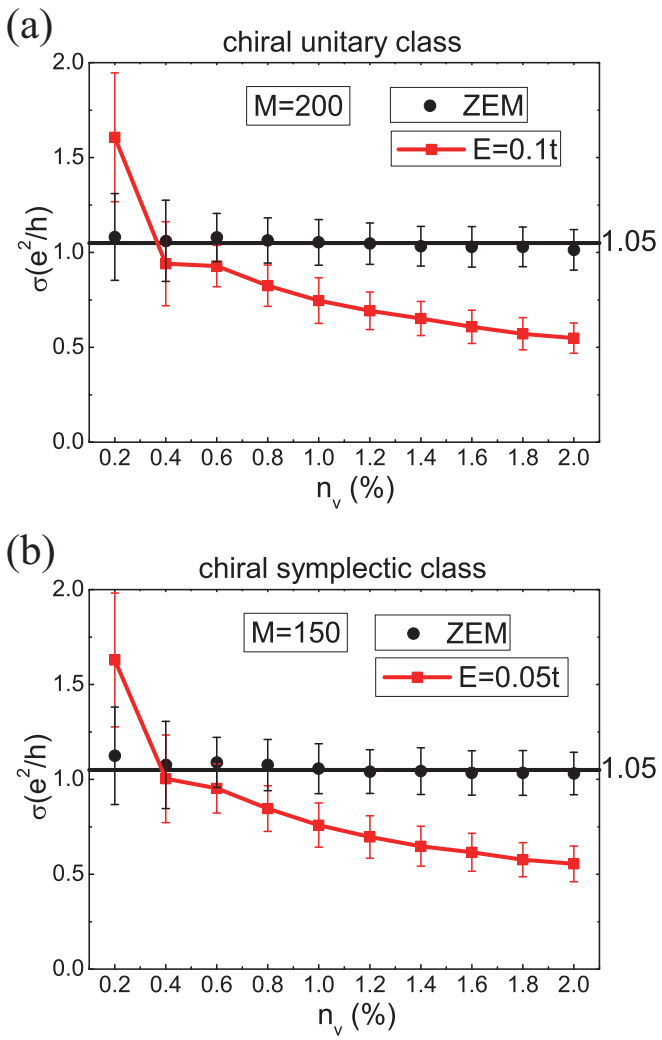

FIG. 8. (a) Longitudinal conductivities of disordered class-AIII Dirac semimetals with $2\times200\times200$ sites as functions of the vacancy concentrations n_v. The black round dots correspond to the CZEM conductivities at the Dirac point. The red squares correspond to the case of the Fermi energy $E_F = 0.1t$. (b) Longitudinal conductivities of disordered class-CII Dirac semimetals with $2\times150\times150$ sites as functions of the vacancy concentrations n_v. The black round dots correspond to the CZEM conductivities at the Dirac point. The red squares correspond to the case of the Fermi energy $E_F = 0.05t$. For both systems, the number of moments of Chebyshev polynomials N is set to 1000 for the cases of $n_v = 0.2\%$ and 0.4%, whereas $N = 500$ for all other vacancy concentrations. The error bars represent the standard deviation due to disorder average.

Appendix) become less and less sparse, and the numerical processes lose more precisions.

Note that the exact robustness property of the CZEM conductivities requires the thermodynamic limit (i.e., $\Omega \to \infty$). Because only finite-size systems can be dealt with for numerical computations, we need to perform numerical scaling by calculating results for increasingly larger sample sizes, so that we can extrapolate the properties of the CZEMs to the thermodynamic limit. In Fig. 7, we display the CZEM conductivities as functions of sample sizes. It can be seen that the CZEM conductivities (black round dots) of both chiral systems do not change with the sample sizes for the numbers of sites ranging from 20 000 to 80 000, and almost remain a constant, namely, $\sigma_{\text{CZEM}} \approx 1.05\frac{e^2}{h}$. This result further suggests that the robustness of the CZEM conductivities is an universal and intrinsic property of the systems.

In Fig. 7, we also plot the size dependencies of conductivities for nonzero Fermi energies (red squares). It is worth noting that this scaling invariance is also valid in a small energy range around the Dirac point, for both models. This result is similar to the delocalization of disordered graphene demonstrated by Zhang *et al.* [3].

Next, we consider the effects of the vacancy disorder itself. The disorder strength can be characterized by the vacancy

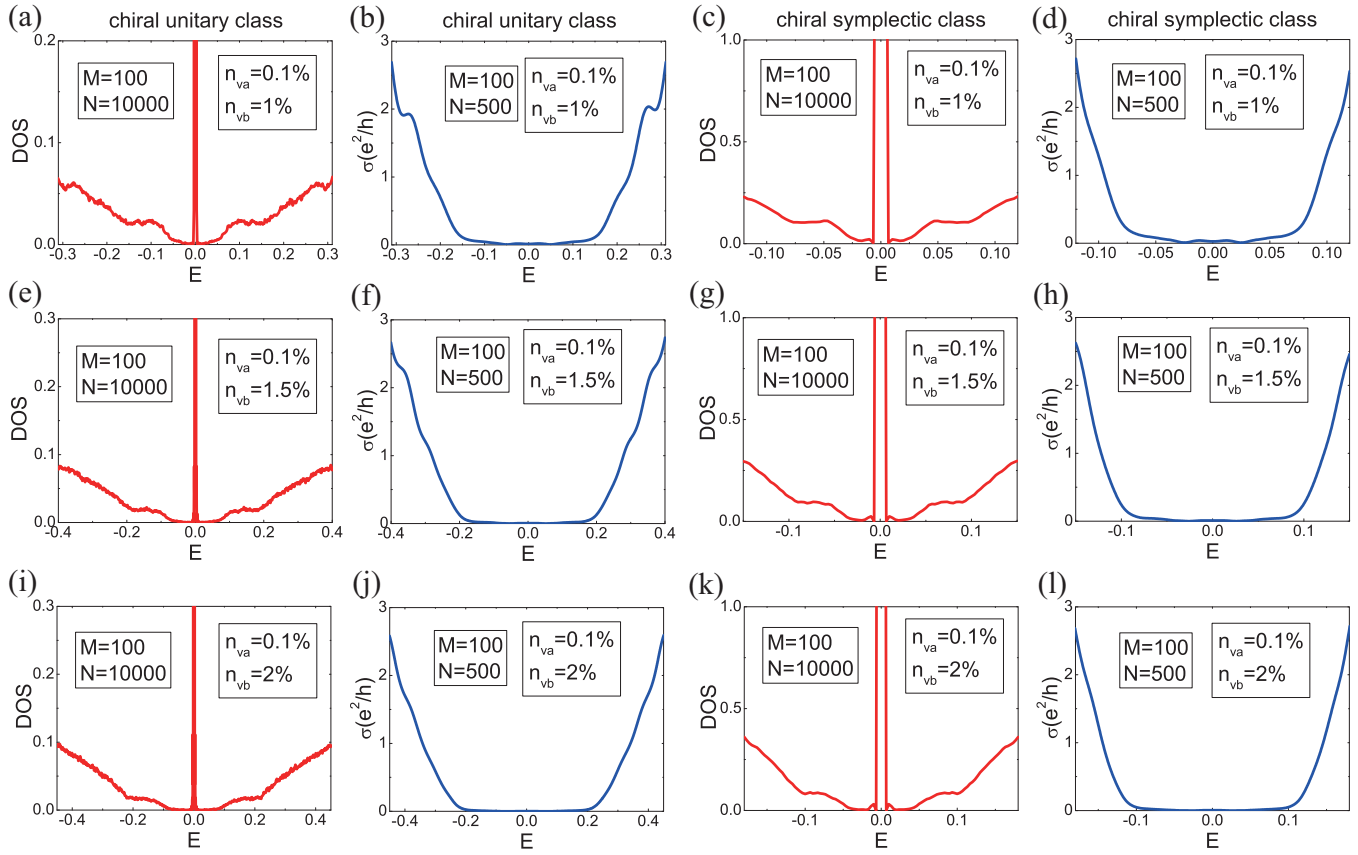

FIG. 9. [(a), (e), and (i)] DOS of disordered class-AIII Dirac semimetals as functions of the energy for (a) the vacancy concentrations of the sublattice A $n_{va} = 0.1\%$ and the sublattice B $n_{vb} = 1\%$, (e) $n_{va} = 0.1\%$ and $n_{vb} = 1.5\%$, and (i) $n_{va} = 0.1\%$ and $n_{vb} = 2\%$. [(b), (f), and (j)] Longitudinal conductivities of disordered class-AIII Dirac semimetals as functions of the Fermi energy for (b) $n_{va} = 0.1\%$ and $n_{vb} = 1\%$, (f) $n_{va} = 0.1\%$ and $n_{vb} = 1.5\%$, and (j) $n_{va} = 0.1\%$ and $n_{vb} = 2\%$. [(c), (g), and (k)] DOS of disordered class-CII Dirac semimetals as functions of the energy for (c) $n_{va} = 0.1\%$ and $n_{vb} = 1\%$, (g) $n_{va} = 0.1\%$ and $n_{vb} = 1.5\%$, and (k) $n_{va} = 0.1\%$ and $n_{vb} = 2\%$. [(d), (h), and (l)] Longitudinal conductivities of disordered class-CII Dirac semimetals as functions of the Fermi energy for (d) $n_{va} = 0.1\%$ and $n_{vb} = 1\%$, (h) $n_{va} = 0.1\%$ and $n_{vb} = 1.5\%$, and (l) $n_{va} = 0.1\%$ and $n_{vb} = 2\%$. For both systems, the samples have $2\times100\times100$ sites. The number of moments of Chebyshev polynomials N is set to 10000 for DOS, and $N = 500$ for longitudinal conductivities.

concentrations n_v. To investigate the influences of the disorder strength on the CZEM conductivity, we numerically compute the longitudinal conductivities at the Dirac points for different vacancy concentrations ranging from 0.2% to 2%. As shown in Fig. 8 (black round dots), the CZEM conductivity almost remains constant (i.e., $\sigma_{\text{CZEM}} \approx 1.05\frac{e^2}{h}$) over an order of magnitude in n_v, except that, for the weak disorder strength (namely, the dilute vacancy concentration), the CZEM conductivity slightly increases as the vacancy concentration decreases. Our physical understandings of this behavior are as follows.

Strictly speaking, the Kubo conductivity of CZEM requires the thermodynamic limit. In other words, we *first* need to take the limit $\Omega \to \infty$ and *then* set the energy broadening parameter $\eta \to 0$. Since the biggest possible size Ω of the system is restricted by numerical practicalities, the smallest possible η must be a finite value. According to the fact that the momentum relaxation time τ associated with vacancy scattering is smaller than $\hbar/\eta$ [29,50] (i.e., $\tau \lesssim \hbar/\eta$), and, at the same time, inversely proportional to the vacancy concentration n_v [51] (i.e., $\tau \propto \frac{1}{n_v}$), the numerical computation requires a smaller η for a smaller n_v. Recall that smaller η means greater N (i.e., the number of moments of Chebyshev polynomials), which is computationally more expensive. Thus, for small n_v, our results may have errors due to our limited computational capability of high-performance computing. Consequently, for the case of $n_v = 0.2\%$, although we use a greater N (namely, $N = 1000$), the CZEM conductivity is slightly greater than those for other cases of vacancy concentrations, as shown in Fig. 8 (black round dots). However, the CZEM conductivity almost remains constant for n_v ranging from 0.4% to 2%. Note that we also use $N = 1000$ for $n_v = 0.4\%$.

For comparison, in Fig. 8 (red squares) we also plot the conductivities as functions of n_v for $E_F = 0.1t$ in the class AIII Dirac semimetals and for $E_F = 0.05t$ in the class CII Dirac semimetals. The results display that, near the Dirac points, the conductivities remarkably decrease with increasing the vacancy concentration, showing prominent localization.

Another interesting fact is that the CZEM exists for each disordered sample. Our numerical results show that there is a δ-function-like peak of DOS at the Dirac point for each sample of both systems. Moreover, for all samples, the conductivities at zero energy are larger than $0.6\frac{e^2}{h}$, in spite of statistical

fluctuations. These facts imply the presence of nonlocalized states with zero energy. For a Dirac matter with chiral disorder, the chiral symmetry protects CZEMs from localization associated with strong quantum interference effects at the Dirac point. In other words, the chiral symmetry is a necessary condition for the reality of CZEMs. The nature of the highly delocalized CZEMs protected by the chiral symmetry is robust against the variation of the sample sizes, the vacancy concentrations, and the numbers of moments of Chebyshev polynomials. On the other hand, for vacancy-defective graphene (chiral orthogonal class, i.e., the class BDI), numerical results show that the CZEM conductivity is $\frac{4e^2}{\pi h}$ [13]. The CZEM conductivities are of the order of $\frac{e^2}{h}$ for all three Chiral classes. The slight difference between $1.05\frac{e^2}{h}$ for the classes AIII and CII and $\frac{4e^2}{\pi h}$ for the class BDI implies that the CZEM conductivities depend weakly on the Chiral classes. A better understanding of this dependence remains an open question. Investigation in this direction is currently in progress.

Finally, we numerically investigate the localization of the classes AIII and CII Dirac semimetals for the case that the vacancy concentrations are different in the two sublattices, i.e., $n_{va} \neq n_{vb}$. Figure 9 shows DOS and longitudinal conductivities as functions of the energy for different vacancy concentration differences $|n_{va} - n_{vb}|$. The results display that the CZEM conductivity vanishes, as shown in Figs. 9(b), 9(d) 9(f), 9(h), 9(j), and 9(l). Hence, both kinds of disordered chiral systems exhibit localization at the Dirac point. Moreover, a mobility gap in the conductivity curve opens around the Dirac point. The width of the mobility gap is increasing with larger vacancy concentration difference $|n_{va} - n_{vb}|$. In addition, as shown in Figs. 9(a), 9(e), 9(i), 9(c), 9(g), and 9(k), a band gap in the DOS emerges around zero energy. This numerical result is consistent with the result predicted by the renormalization group analysis of the nonlinear sigma model for a 2D chiral metal (bipartite lattice) with vacancy [12]. On the other hand, within the band gap, there is a δ-function-like peak of DOS at the Dirac point, which is due to the presence of numerous localized states with zero energy. Furthermore, the width of the mobility gap is evidently larger than that of the band gap. This result indicates that there are plenty of localized states existing not only at the Dirac point but also in the band tails of the valence and conduction bands.

IV. CONCLUSIONS

In summary, we have numerically investigated the vacancy-induced CZEMs of the classes AIII and CII disordered Dirac semimetals on a 2D square bipartite lattice using the Kubo-Greenwood formula with the KPM method. It is found that, for both systems, the CZEMs exhibit the critical delocalization. The CZEM conductivity remains a robust constant, i.e., $\sigma_{\mathrm{CZEM}} \approx 1.05\frac{e^2}{h}$. It is insensitive to the sample sizes, the vacancy concentrations, and the numbers of moments of Chebyshev polynomials. The CZEM conductivity is almost the same for both kinds of disordered chiral systems. However, it is not equal to that of graphene (namely, $\frac{4e^2}{\pi h}$), which belongs to the class BDI with 2D hexagonal bipartite lattice. Furthermore, for the case that the vacancy concentrations are different in the two sublattices, the CZEM conductivity vanishes, and thus both kinds of disordered chiral systems exhibit localization at the Dirac point. In addition, the band gap and the mobility gap open around the Dirac point. There is a δ-function-like peak of DOS at the Dirac point within the band gap and the width of the mobility gap is greater than that of the band gap, because of the presence of numerous localized states at the Dirac point and in the band tails of the valence and conduction bands.

ACKNOWLEDGMENTS

This work was supported by the National Natural Science Foundation of China (Grants No. 11374294, No. 61427901, No. 61176089, No. 10974043, No. 11004046, and No. 11474084), the Natural Science Foundation of Hebei Province (Grant No. A2012205071), and the Foundation of Shijiazhuang University (Grant No. XJPT002). The calculations were performed in high-performance computing facilities at National Supercomputing Centers in Shanghai and Shenzhen.

APPENDIX: KERNEL POLYNOMIAL METHOD IN A NUTSHELL

Most linear response functions can be expressed in terms of Green's functions. However, the degrees of freedom of mesoscopic systems are usually so huge that numerical treatments of the associated matrices are almost impossible. Fortunately, for the numerical calculations of huge matrices, the kernel polynomial method (KPM) is a very efficient and stable algorithm [38,39,52–55]. According to KPM, the Green's functions can be expanded as the first kind Chebyshev polynomials of the Hamiltonian matrices. As a kind of orthogonal polynomials, Chebyshev polynomials are defined on the real interval $[-1,1]$. The Chebyshev polynomials of first kind $T_n(x)$ can be expressed in the explicit form

$$T_n(x) = \cos[n \arccos(x)], \tag{A1}$$

and obey the recursion relations,

$$\begin{aligned} T_0(x) &= 1, \\ T_{-1}(x) &= T_1(x) = x, \\ T_{n+1}(x) &= 2xT_n(x) - T_{n-1}(x). \end{aligned} \tag{A2}$$

In KPM, the Chebyshev expansions of the Green's functions possess good convergence properties. What is more, after long time practices of numerical calculations, it turned out that applying optimal kernels, i.e., attaching appropriate auxiliary coefficients g_n to Chebyshev polynomials, can damp down the Gibbs oscillations [56,57], which occur near discontinuities or singularities of the expanded function for a truncation of the infinite Chebyshev polynomial series. In addition, in KPM, most of the numerical calculations associated with the Green's functions or spectral functions can be translated into matrix-vector multiplication for the sparse Hamiltonian matrices, taking advantage of the sparse matrix methods and parallel algorithms.

According to KPM, an arbitrary function defined on a finite interval can be expanded in terms of Chebyshev polynomials

of first kind,

$$f_{\mathrm{KPM}}(x)=\frac{1}{\pi\sqrt{1-x^2}}\left[g_0\mu_0+2\sum_{n=1}^{N-1}g_n\mu_nT_n(x)\right], \quad \text{(A3)}$$

where $\mu_n=\int_{-1}^{1}f(x)T_n(x)dx$ indicate the expansion coefficients, N is the truncation number of moments of Chebyshev polynomials, and g_n denote the optimal kernels [38,55]. In this work, we use the Jackson kernel

$$g_n=\frac{(N-n+1)\cos\frac{\pi n}{N+1}+\sin\frac{\pi n}{N+1}\cot\frac{\pi}{N+1}}{N+1}. \quad \text{(A4)}$$

By using the expression (A3), both the δ function and the Green function can be expanded in terms of the Chebyshev polynomials

$$\delta(\tilde{\varepsilon}-\tilde{H})=\frac{2}{\pi a\sqrt{1-\tilde{\varepsilon}^2}}\sum_{n=0}^{N}\frac{1}{\delta_{n,0}+1}g_nT_n(\tilde{H})T_n(\tilde{\varepsilon}), \quad \text{(A5)}$$

$$G^{\pm}(\tilde{\varepsilon},\tilde{H})=\mp\frac{2i}{a\sqrt{1-\tilde{\varepsilon}^2}}\sum_{n=0}^{N}g_n\frac{e^{\mp in\arccos(\tilde{\varepsilon})}}{\delta_{n,0}+1}T_n(\tilde{H}). \quad \text{(A6)}$$

Substituting Eqs. (A5) and (A6) into Eqs. (9) and (8) given in main text, respectively, we obtain the Chebyshev expansions of the DOS and longitudinal conductivity:

$$\rho(\tilde{\varepsilon})=\frac{2\xi}{\pi a\sqrt{1-\tilde{\varepsilon}^2}}\frac{1}{D}\sum_{n=0}^{N}g_n\frac{g_n}{\delta_{n,0}+1}\mathrm{Tr}[T_n(\tilde{H})]T_n(\tilde{\varepsilon}), \quad \text{(A7)}$$

$$\sigma_{xx}(\tilde{E}_F)=\frac{4\xi\hbar e^2}{\pi a^2(1-\tilde{\varepsilon}^2)\Omega}\sum_{n,m=0}^{N}[T_n(\tilde{E}_F)T_m(\tilde{E}_F)\mu_{nm}], \quad \text{(A8)}$$

$$\mu_{nm}=\frac{g_ng_m}{(\delta_{n,0}+1)(\delta_{m,0}+1)}\mathrm{Tr}[v_xT_n(\tilde{H})v_xT_m(\tilde{H})], \quad \text{(A9)}$$

where $\xi=1,2$. For the class AIII Dirac semimetals, we set $\xi=2$ due to spin degeneracy. For the class CII Dirac semimetals, we set $\xi=1$ arising from the removal of spin degeneracy.

Chebyshev polynomials are defined on the real interval $[-1,1]$, whereas the eigenvalue spectrums of the Hamiltonian matrices we are interested in do not fit into this interval in general. To rescale the Hamiltonian H and energies ε to the interval $[-1,1]$, we therefore have to apply a linear transformation and denote all rescaled physical quantities with a tilde,

$$\tilde{H}=\frac{H-b}{a},\quad \tilde{\varepsilon}=\frac{\varepsilon-b}{a}, \quad \text{(A10)}$$

with the scaling factors of the form

$$a=\frac{E_{\max}-E_{\min}}{2-\zeta},\quad b=\frac{E_{\max}+E_{\min}}{2}, \quad \text{(A11)}$$

where, $E_{\min}$ and $E_{\max}$ indicate the lower and upper bounds of the eigenvalue spectra, which can be calculated by using the FEAST algorithm of the latest version of Intel MKL. The parameter ζ is a infinitesimal cutoff introduced to guarantee the numerical stability. We set a fixed value $\zeta=0.0001$ in our numerical calculation.

From Eqs. (A7) and (A9), the calculations of the DOS and longitudinal conductivity require traces over the whole Hilbert space. For a D-dimensional matrix, the resource consumption of numerical computation is proportional to D^2. The numerical calculation is thus computationally expensive for the case of huge matrices. Fortunately, instead of complete trace summations, the expansion coefficients of the DOS and longitudinal conductivity can be calculated with the random phase vector approximation [38,40,56,58], i.e., stochastic evaluation of traces, for large sparse matrices. In this method, a set of random complex vectors can be constructed as

$$|r\rangle=\sum_{i=1}^{D}\xi_{ri}|i\rangle,\quad r=1,2,\ldots,R, \quad \text{(A12)}$$

with a small number of random vectors $R\ll D$, where, $|i\rangle$ denotes a set of arbitrary basis vectors, the coefficients ξ_{ri} are a set of independent uniformly distributed random complex numbers $\xi_{ri}\in C$, which possess the following characteristics,

$$\langle\langle\xi_{ri}\rangle\rangle=0,\quad \langle\langle\xi^*_{ri}\xi_{r'i'}\rangle\rangle=\delta_{rr'}\delta_{ii'}, \quad \text{(A13)}$$

where $\langle\langle\cdots\rangle\rangle$ indicates the statistical average. In general, the statistical error can be reduced by choosing $\xi_{ri}=e^{i\phi}$ with $\phi\in[0,2\pi]$ as a set of equally distributed random phases [40,56,59]. For huge sparse matrices, the full traces in Eqs. (A7) and (A9) can be replaced by the statistical expected values in terms of the random vectors,

$$\mathrm{Tr}[T_n(\tilde{H})]\approx\frac{1}{R}\sum_{r=1}^{R}\langle r|T_n(\tilde{H})|r\rangle, \quad \text{(A14)}$$

$$\mathrm{Tr}[v_xT_n(\tilde{H})v_xT_m(\tilde{H})]\approx\frac{1}{R}\sum_{r=1}^{R}\langle r|v_xT_n(\tilde{H})v_xT_m(\tilde{H})|r\rangle. \quad \text{(A15)}$$

The resource consumption required to numerically calculate (A14) and (A15) is now proportional to $D\times R$ instead of D^2. It can be proved that the relative error of the stochastic trace estimate is of order $O(1/\sqrt{RD})$ [38,40]. That is to say, the error of this approximation reduces with increasing the product of the number of random vectors R and the dimension of matrix D. Therefore only a few random vectors are necessary for large systems. For systems with ten thousands of lattice sites considered in this work, we find that setting $R=24$ is enough to yield a good precision.

[1] P. W. Anderson, Phys. Rev. **109**, 1492 (1958)

[2] Y. Y. Zhang, R. L. Chu, F. C. Zhang, and S. Q. Shen, Phys. Rev. B **85**, 035107 (2012).

[3] Y. Y. Zhang, Jiangping Hu, B. A. Bernevig, X. R. Wang, X. C. Xie, and W. M. Liu, Phys. Rev. Lett. **102**, 106401 (2009).

[4] Y. Y. Zhang, W. F. Tsai, K. Chang, X. T. An, G. P. Zhang, X. C. Xie, and S. S. Li, Phys. Rev. B **88**, 125431 (2013).

[5] J. H. Pixley, P. Goswami, and S. Das Sarma, Phys. Rev. Lett. **115**, 076601 (2015).

[6] F. Evers and A. D. Mirlin, Rev. Mod. Phys. **80**, 1355 (2008).

[7] C. W. J. Beenakker, Rev. Mod. Phys. **69**, 731 (1997).
[8] M. R. Zirnbauer, J. Math. Phys. (NY) **37**, 4986 (1996).
[9] A. Altland and M. R. Zirnbauer, Phys. Rev. B **55**, 1142 (1997).
[10] C. K. Chiu, J. C. Y. Teo, A. P. Schnyder, and S. Ryu, Rev. Mod. Phys. **88**, 035005 (2016).
[11] Y. Hatsugai, T. Morimoto, T. Kawarabayashi, Y. Hamamoto, and H. Aoki, New J. Phys. **15**, 035023 (2013).
[12] P. M. Ostrovsky, I. V. Protopopov, E. J. König, I. V. Gornyi, A. D. Mirlin, and M. A. Skvortsov, Phys. Rev. Lett. **113**, 186803 (2014).
[13] A. Ferreira and E. R. Mucciolo, Phys. Rev. Lett. **115**, 106601 (2015).
[14] N. Weik, J. Schindler, S. Bera, G. C. Solomon, and F. Evers, Phys. Rev. B **94**, 064204 (2016).
[15] G. Santhosh, V. Sreenath, A. Lakshminarayan, and R. Narayanan, Phys. Rev. B **85**, 054204 (2012).
[16] X. Fan, W. Huang, T. X. Ma, and L. G. Wang, Phys. Rev. B **93**, 165137 (2016).
[17] A. Cresti, F. Ortmann, T. Louvet, D. Van Tuan, and S. Roche, Phys. Rev. Lett. **110**, 196601 (2013).
[18] S. D. Wu, L. Jing, Q. X. Li, Q. W. Shi, J. Chen, H. B. Su, X. P. Wang, and J. L. Yang, Phys. Rev. B **77**, 195411 (2008).
[19] N. M. R. Peres, S. W. Tsai, J. E. Santos, and R. M. Ribeiro, Phys. Rev. B **79**, 155442 (2009).
[20] M. I. Katsnelson, Eur. Phys. J. B **51**, 157 (2006).
[21] K. S. Novoselov, A. K. Geim, S. V. Morozov, D. Jiang, M. I. Katsnelson, I. V. Grigorieva, S. V. Dubonos, and A. A. Firsov, Nature (London) **438**, 197 (2005).
[22] S. V. Morozov, K. S. Novoselov, M. I. Katsnelson, F. Schedin, L. A. Ponomarenko, D. Jiang, and A. K. Geim, Phys. Rev. Lett. **97**, 016801 (2006).
[23] R. V. Gorbachev, F. V. Tikhonenko, A. S. Mayorov, D. W. Horsell, and A. K. Savchenko, Phys. Rev. Lett. **98**, 176805 (2007).
[24] J. Tworzydło, B. Trauzettel, M. Titov, A. Rycerz, and C. W. J. Beenakker, Phys. Rev. Lett. **96**, 246802 (2006).
[25] K. Nomura and A. H. MacDonald, Phys. Rev. Lett. **96**, 256602 (2006).
[26] T. Ando, J. Phys. Soc. Jpn. **75**, 074716 (2006).
[27] J. Martin, N. Akerman, G. Ulbricht, T. Lohmann, J. H. Smet, K. von Klitzing, and A. Yacoby, Nat. Phys. **4**, 144 (2008).
[28] Y. Zhang, V. W. Brar, C. Girit, A. Zettl, and M. F. Crommie, Nat. Phys. **5**, 722 (2009).
[29] M. Trushin, J. Kailasvuori, J. Schliemann, and A. H. MacDonald, Phys. Rev. B **82**, 155308 (2010).
[30] Z. G. Song, Y. Y. Zhang, J. T. Song, and S. S. Li, Sci. Rep. **6**, 19018 (2016).
[31] T. Kawarabayashi, H. Aoki, and Y. Hatsugai, Phys. Rev. B **94**, 235307 (2016).
[32] L. H. Li and M. A. N. Araújo, Phys. Rev. B **94**, 165117 (2016).
[33] T. Habe, Phys. Rev. B **95**, 115405 (2017).
[34] C. Beenakker, Science **353**, 539 (2016).
[35] Z. Wu, L. Zhang, W. Sun, X. T. Xu, B. Z. Wang, S. C. Ji, Y. J. Deng, S. Chen, X. J. Liu, and J. W. Pan, Science **354**, 83 (2016).
[36] J. M. Hou, Phys. Rev. Lett. **111**, 130403 (2013).
[37] S. M. Young and C. L. Kane, Phys. Rev. Lett. **115**, 126803 (2015).
[38] A. Weiße, G. Wellein, A. Alvermann, and H. Fehske, Rev. Mod. Phys. **78**, 275 (2006).
[39] J. P. Boyd, *Chebyshev and Fourier Spectral Methods*, 2nd ed. (Dover, New York, 2001).
[40] J. H. García, L. Covaci, and T. G. Rappoport, Phys. Rev. Lett. **114**, 116602 (2015).
[41] L. Covaci, F. M. Peeters, and M. Berciu, Phys. Rev. Lett. **105**, 167006 (2010).
[42] R. Kubo, J. Phys. Soc. Jpn. **12**, 570 (1957).
[43] R. Kubo, M. Yokota, and S. J. Nakajima, J. Phys. Soc. Jpn. **12**, 1203 (1957).
[44] A. Crepieux and P. Bruno, Phys. Rev. B **64**, 014416 (2001).
[45] D. A. Greenwood, Proc. Phys. Soc. London **71**, 585 (1958).
[46] P. Stieda, J. Phys. C: Solid State Phys. **15**, L717 (1982).
[47] H. Jiang, S. G. Cheng, Q. F. Sun, and X. C. Xie, Phys. Rev. Lett. **103**, 036803 (2009).
[48] A. H. Castro Neto, F. Guinea, and N. M. R. Peres, Rev. Mod. Phys. **81**, 109 (2009).
[49] P. M. Ostrovsky, I. V. Gornyi, and A. D. Mirlin, Phys. Rev. B **74**, 235443 (2006).
[50] D. C. Licciardello and D. J. Thouless, J. Phys. C **8**, 4157 (1975).
[51] Y. V. Nazarov and Y. M. Blanter, *Quantum Transport: Intoduction to Nanoscience* (Cambridge University Press, New York, 2009).
[52] A. Weiße, Eur. Phys. J. B **40**, 125 (2004).
[53] A. F. Voter, J. D. Kress, and R. N. Silver, Phys. Rev. B **53**, 12733 (1996).
[54] H. Röder, R. N. Silver, D. A. Drabold, and J. J. Dong, Phys. Rev. B **55**, 15382 (1997).
[55] R. N. Silver, H. Röder, A. F. Voter, and J. D. Kress, J. Comput. Phys. **124**, 115 (1996).
[56] R. N. Silver and H. Röder, Int. J. Mod. Phys. C **5**, 735 (1994).
[57] L. W. Wang, Phys. Rev. B **49**, 10154 (1994).
[58] D. A. Drabold and O. F. Sankey, Phys. Rev. Lett. **70**, 3631 (1993).
[59] T. Iitaka and T. Ebisuzaki, Phys. Rev. E **69**, 057701 (2004).